# PHOTONIC CRYSTAL ENHANCED MICROSCOPY FOR IMAGING OF LIVE CELL ADHESION

BY

WEILI CHEN

THESIS

Submitted in partial fulfillment of the requirements
for the degree of Master of Science in Electrical and Computer Engineering
in the Graduate College of the
University of Illinois at Urbana-Champaign, 2014

Urbana, Illinois

Advisor:

Professor Brian T. Cunningham

## ABSTRACT

A form of microscopy based on the unique optical properties of a photonic crystal (PC) biosensor provides both label-free (LF) and enhanced fluorescence (EF) imaging modalities for the study of cell-surface interactions and nanoparticle-based assays. The imaging system utilizes an angle-tunable illumination source, either LED or laser, to achieve highly efficient coupling of incident light to PC optical resonances. Detection of the wavelength of resonantly reflected light from PC surfaces enable high-sensitivity label-free biosensing, whereas the enhanced electromagnetic (EM) fields associated with the resonances can be used to strongly improve the fluorescence output of fluorescent labels above PC surfaces.

Photonic Crystal Enhanced Microscopy (PCEM) was applied to the study of murine dental stem cells by providing label-free, quantitative, submicron resolution, time-resolved images of the evolution of cell attachment and morphology during chemotaxis and drug-induced apoptosis. It enabled the monitoring of cell behavior with spatial resolution sufficient for observing intracellular attachment strength gradients. PCEM was also used to image fluorescence labeled cells, in which alternating on/off-resonance images was used to derive maps of the surface engagement of cell structures.

## ACKNOWLEDGMENTS

First of all, I would like to thank my advisor Professor Brian T. Cunningham for giving me the opportunity to work in one of the best engineering schools in the world. Without his valuable guidance and firm support, it would be impossible for me to overcome all the difficulties in this research project and write this thesis to sum up my research results obtained in the last two years.

I also wish to acknowledge several past and present members of the Nano Sensors Research Group: Dr. Meng Lu, Dr. Vikram Chaudhery, Dr. Erich Lidstone, Dr. Anusha Pokhriyal, James Polans, Yafang Tan, Kenny Long and Hojeong Yu. The experience and knowledge selflessly shared by them lay a strong foundation for any achievement that I could accomplish. Also, I am thankful for all the staff members in the Micro and Nanotechnology Laboratory who provided us a first-class working environment.

I am thankful for the funding support by National Science Foundation (NSF) under CBET 11-32301 and Grant No. 1254738.

I am deeply grateful for my parents. The things I learned from them: the spirit of enterprise, responsibility, kindness and firmness are the rocks of my professional life. Their encouragement makes me feel fearless for the future and they are always in my heart.

Thanks for both the good times and hard times.

## TABLE OF CONTENTS

## LIST OF ABBREVIATIONS

| | |
|---|---|
| 1D | one-dimensional |
| 2D | two-dimensional |
| API | application programming interface |
| CCD | charge-coupled device |
| Cy-5 | cyanine-5 |
| DIC | differential interference contrast |
| DNA | deoxyribonucleic acid |
| ECM | extracellular matrix |
| EF | enhanced fluorescence |
| EM | electron multiplier |
| FWHM | full width at half maximum |
| LF | label-free |
| NA | numerical aperture |
| PBS | polarizing beamsplitter |
| PC | photonic crystal |
| PCEM | photonic crystal enhanced microscopy |
| PDMS | polydimethylsiloxane |
| PWV | peak wavelength value |
| PIV | peak intensity value |
| Q-factor | quality factor |

| | |
|---|---|
| RCWA | rigorous coupled-wave analysis |
| RI | refractive index |
| RIU | refractive index unit |
| RNA | ribonucleic acid |
| SA | streptavidin |
| SPR | surface plasmon resonance |
| SPRi | surface plasmon resonance imaging |
| TE | transverse electric |
| TIRF | total internal reflection fluorescence |
| TM | transverse magnetic |
| UV | ultraviolet |
| UVCP | ultraviolet cured polymer |

# CHAPTER 1

## INTRODUCTION

The development of cell biology is highly dependent on the progress in light microscopy technology. Such kind of strong correlation comes from two simple facts: (1) vision is one of the most fundamental means that people sense the outside world; (2) cellular level biological structures are usually invisibly small for naked eyes. The observations made through early microscopes helped scientists build the foundation of modern biological sciences. As a matter of fact, the biological concept "cell" was firstly brought up by an English microscopist Robert Hooke in the $17^{th}$ century in his famous study of thin slices of cork, which marks the start of imaging in biology. Nowadays, light microscopy has gone far beyond the qualitative viewing of small objects by objective magnification and contrast enhancement. It is possible now to detect the location, motion and environment of specific biomolecular structures, such as proteins and organelles.

The study of cell adhesion is of fundamental importance in cell biology since cell adhesion plays a critical role in a wide range of cellular processes such as growth, migration, proliferation, apoptosis, and differentiation that occur during drug exposure, cell-to-cell communication [1], the presence of chemical gradients [2], introduction of growth factors, and programmed gene expression. Ultimately, these fundamental processes govern biological activity such as tissue growth, inflammation, wound healing and metastasis [3] as cellular adhesion is

modulated by a complex combination of mechanical force from substrate to cell, signaling pathways that involve protein structures embedded in the plasma membrane, the makeup of extracellular matrix (ECM) proteins, and cytoskeleton components of the cell [4]. While the significance of cell-substrate adhesion has been realized for years, there are few tools currently available that enable visualization and quantification of this phenomenon with the ability to screen out the effects of cell-to-surface coupling behavior.

In this thesis, we will present photonic crystal enhanced microscopy (PCEM) as both a label-free biosensor imaging technique and a surface-restricted fluorescence imaging technique for visualizing and quantifying complex cellular responses to multiple stimuli over prolonged periods of study.

## 1.1 Optical Microscopy

Optical microscope is now one of the most widely used tools in biomedical research for various imaging purposes with the ability to magnify the object of observation. While people have realized the magnification effect brought by lens-shaped crystals or glass from long ago, technically the first compound microscope was not invented until the late $15^{th}$ century [5]. Compared to the simple microscope, which relies on a single lens to provide an erect enlarged virtual image, the compound microscope comprised of two or more convex lenses in a tube allows for much higher magnification and more flexibility to adjust the magnification. The lower lens, called the objective lens, is put close

to the object to be observed and collects the light that focuses a real image of the object inside the microscope. This image is then magnified by the upper lens, called the eyepiece, and forms an enlarged inverted virtual image of the object. The overall magnification effect of the compound microscope is the product of the lateral magnification caused by the objective and the angular magnification caused by the eyepiece. Meanwhile, the image resolution of compound microscope is limited by light diffraction. Because objective with certain numerical aperture (NA) can only collect finite information about the object, the output image of a single point source, instead of being a point, is a circle with certain radius, called Airy disks [6]. The resolution of a compound microscope is defined as the ability to distinguish two closely spaced Airy disks, therefore it is commonly stated as the radius of the Airy disk, which is the ratio between half the wavelength of the applied light and the numerical aperture. While great progress has been made in modern microscopy technologies with various kinds of high quality images generated by microscopes today, the principles of the compound microscope remain as the underlying foundation for all of them.

Except for the fluorescence microscopy that we are going to introduce in more details in the Section 1.2, there are several types of optical microscopy techniques that are commonly used in biology research, including bright field, dark field, phase contrast, differential interference contrast (DIC) and confocal microscopy. Bright field microscopy, as the simplest of all optical microscopy illumination techniques, records the intensity distribution of the white light

scattered by the observed objects, which must be transparent. The image contrast is purely caused by the difference between materials in light absorbance. Dark field microscopy improves the image contrast by blocking low frequency component of the light signal at the cost of big intensity loss, which has the same effect as to add a high pass filter. Phase contrast microscopy, different from the previous two which measure intensity amplitude of light, records phase shifts after the light passing through a transparent sample. It is usually achieved by separating the illuminating background light from the sample scattering light and measuring the interference pattern. DIC also uses the interference effect to form the image but with two orthogonally polarized beams coming from the same light source that both pass through the sample. The image contrast results from the optical path difference of the two beams. Confocal microscopy applies a spatial pinhole to eliminate out-of-focus light coming from the object and scans over the object surface to form the whole image. It theoretically can achieve unlimited image resolution, but the pinhole in practice cannot be made too small.

## 1.2 Fluorescence Microscopy

Fluorescence microscopy is one of the most popular microscopy currently in medical and biological research because of its excellent specificity and high sensitivity as well as the wide availability of fluorophores [7]. In contrast to normal optical microscopy technique, fluorescence microscopy relies on the use of fluorescent probes that emit fluorescence light by themselves under external

stimulus and label the specific structures within biological samples. The electrons of the fluorescent molecules (or fluorophores) can absorb the photons of the excitation light at a specific wavelength, which raises the energy level of the electrons to an excited state. The excited state exists only for a finite time (typically 1-10 nanoseconds). During this period, some of the energy is dissipated subject to multiple interactions with the outside environment. The remaining energy is then emitted as a photon returning the electrons back to the ground state. Since the emitted photons usually carry less energy than the incident ones, the wavelength of emitted fluorescence light is distinct from the incident light. Therefore we can use a filter to block the incident light and only collect the fluorescence light coming from the labeled biological structures. In this way, the fluorescence light can visibly indicate the presence of a structure even if it is too small to be resolved in a compound microscope, making fluorescence microscopy a very powerful tool widely used in many different biomedical research areas, especially in the quantitative measurements of biological structures and processes.

However, the use of fluorescence microscopy is limited by several inherent drawbacks. First, fluorophores lose the ability to emit fluorescence light under continuous illumination in a process called photobleaching. It is caused by the chemical damage of fluorophores from the excited electrons. The rapid intensity decay allows only a limited time for researchers to analyze the objects. Second, the fluorophores are often toxic, especially to living cells. The fluorescent labels frequently permanently alter the state of the cell, and often require fixing or

isolation of the samples to be considered for examination. Third, the natural emitted light coming from unlabeled biological structures known as autofluorescence interfering with specific fluorescent signals can compromise the detection sensitivity. The autofluorescence occurs in many biological structures such as lysosomes as well as some other non-biological structures [8].

One particular form of fluorescence microscopy, total internal reflection fluorescence (TIRF) microscopy (shown in Fig. 1), can visualize cell-substrate interactions by utilizing fluorescent dyes that label specifically targeted cell structures and by concentrating illumination energy to a confined zone on a transparent glass substrate. The evanescent field generated by the total internal reflection effect can selectively excite fluorophores near the adherent cell surface, while minimizing fluorescence originating from the bulk of the cell [9] through a spatially restricted evanescent field upon a substrate surface. While TIRF microscopy has been broadly adopted through the availability of specialized microscope objectives, the approach is not able to differentiate between a locus of high fluorescence intensity that is bright due to being close to the cell-substrate interface, and a high intensity region of an image that is bright due to the high concentration of fluorescent dye contained [10].

### 1.3 Surface Plasmon Resonance Imaging

In order to address the challenges inherent in label-based cell imaging techniques, label-free microscopy technologies have been demonstrated as

effective tools for measuring an increasingly diverse range of cellular processes [11-13]. Label-free microscopy involves a biosensor transducer surface that generates an electrical or optical signal when cells interact with it. Biosensors measure intrinsic cellular properties (such as dielectric permittivity) that can be used to determine the number of cells in contact with the transducer, or to determine the distribution of focal adhesion points. Such transducers may be prepared with surface coatings that either selectively capture specific cell populations through interaction with proteins expressed on their outer membranes or mimic the in vivo microenvironment within tissues.

Due to the fundamental importance of cell-surface interactions, several technologies have sought to quantify and image cell membrane adhesion. Surface Plasmon Resonance imaging (SPRi) [14] (shown in Fig. 2) is capable of detecting cell attachment to a gold surface by measuring changes in the intensity of front-reflected light at a fixed angle and wavelength, but practical limitations degrade image quality. SPRi requires illumination to pass through cell structures, which introduces changes in reflected light intensity that are not related to cell surface attachment, and the lateral propagation distance of surface plasmons limits spatial resolution [15]. Interpretation of SPRi images is complicated by the variability of reflected light intensity introduced by scattering, inhomogeneity of the light source, and nonuniformity of the sensor surface [16], while non-normal light via prism coupling hinders the quality of focus [17].

## 1.4 Photonic Crystal Biosensor

Photonic Crystal (PC) biosensors have recently been demonstrated as a highly versatile technology for a variety of label-free assays including high-throughput screening of small molecule-protein interactions, characterization of protein-protein interactions, and measurement of cell attachment modulation by drugs [18-20]. A PC is a sub-wavelength grating structure consisting of a periodic arrangement of a low refractive index material coated with a high reflective index layer (shown in Fig. 3). When the PC is illuminated with a broadband light source, high-order diffraction modes couple light into and out of the high index layer, destructively interfering with the zeroth-order transmitted light [21]. At a particular resonant wavelength and incident angle, complete interference occurs and no light is transmitted, resulting in 100% reflection efficiency. The resonant wavelength is modulated by the addition of biomaterial upon the PC surface, resulting in a shift to a higher wavelength. The electromagnetic standing wave that is generated at the PC surface during resonant light coupling inhibits lateral propagation, thus enabling neighboring regions on the PC surface to display a distinct resonant wavelength that is determined only by the density of biomaterial attached at that precise location. By measuring the resonant peak wavelength value (PWV) on a pixel-by-pixel basis over a PC surface, an image of cell attachment density may be recorded. PWV images of the PC may be gathered by illuminating the structure with collimated white light through the transparent substrate, while the front surface of the PC is immersed in aqueous media.

The advantages of PC-based surfaces for cell attachment imaging are compelling. As a label-free technology, cell attachment to a PC sensor is measured without the use of dyes or stains, so a population of cells can be measured repeatedly without disrupting their culture environment. The detected output signal is highly quantitative, providing measurements that are repeatable between sensors, instruments, and laboratories without photobleaching. PC biosensors are fabricated from inexpensive materials and require only low intensity illumination from beneath the sensor, so no electrical or physical contact between the sensor and the detection system occurs, and illumination does not pass through the cell body, the cell media, or the liquid-air meniscus of a microplate well. The PC biosensor strictly limits lateral propagation of resonantly coupled light, enabling imaging-based detection with resolution sufficient for measuring subtle variations in cell adhesion strength within a single cell, without needing to pre-tune the sensor to a particular resonant coupling condition, as in SPRi. PC biosensor imaging provides information that is fundamentally different than that provided by an optical microscope, as the sensor responds to local variation in cell attachment strength to the transducer surface. The sensor can be prepared with a variety of surface functionalizations (such as matrix coatings, antibodies, and peptides) and thus can be used as a tool for measuring how cell attachment to surfaces is modulated by drugs, growth factors, or other environmental factors.

## 1.5 Figures

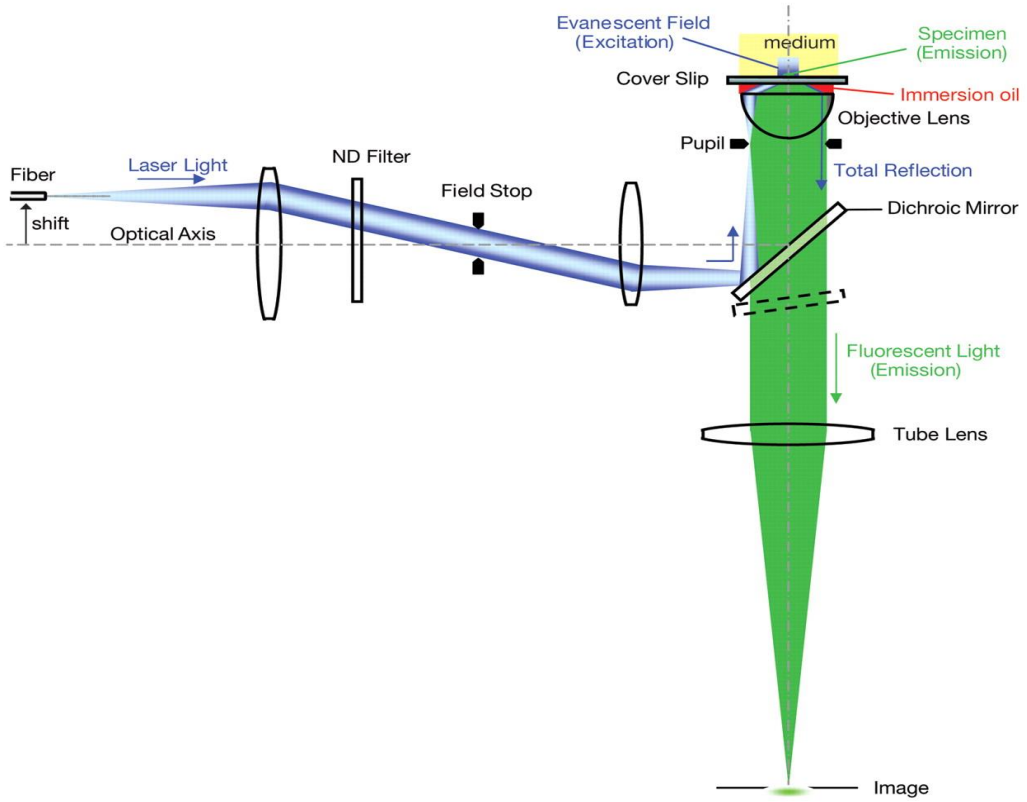


Figure 1 Schematic drawing of a commercially available total internal reflection microscope. A neutral-density (ND) filter can be used to reduce illumination intensity. The collimated beam is then focused on the back focal plane of the objective (in the pupil plane) by a second lens. Moving the fiber laterally results in a corresponding movement of the focused beam in the back focal plane of the objective and a corresponding change in the angle of incidence. The fluorescence emitted by the sample (green) is collected by the objective lens, passes through the dichroic mirror, and is eventually focused on the camera by the tube lens of the microscope [22].

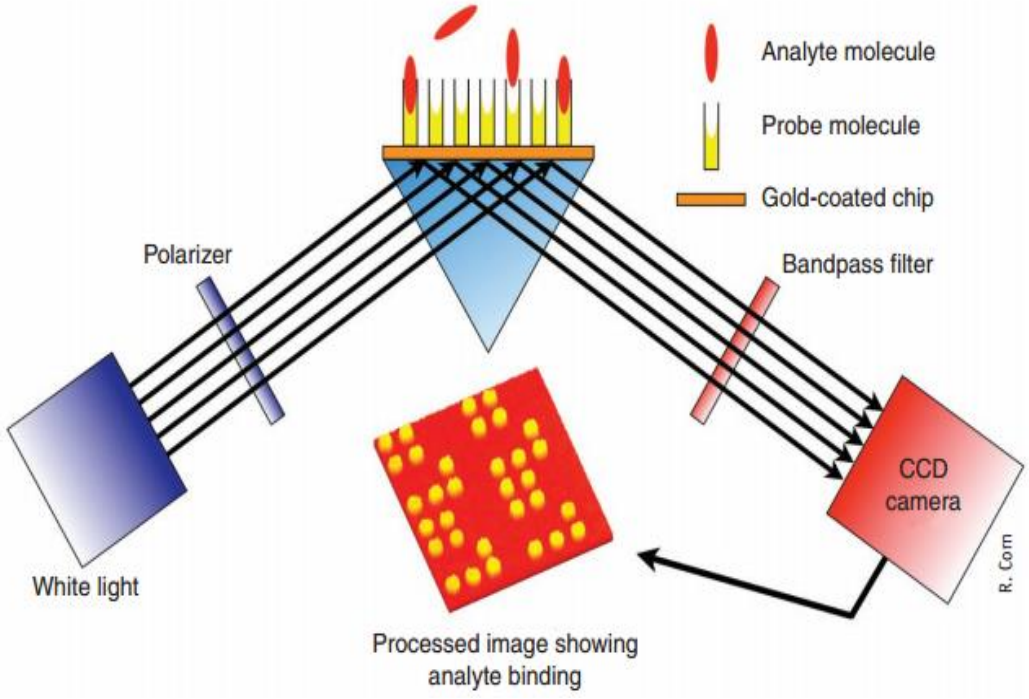


Figure 2 Schematic diagram of surface plasmon resonance imaging (SPRi) setup. SPRi can be used to characterize cell attachment to a metal surface by measuring the induced changes in light reflectivity with both wavelength and angle fixed [23].

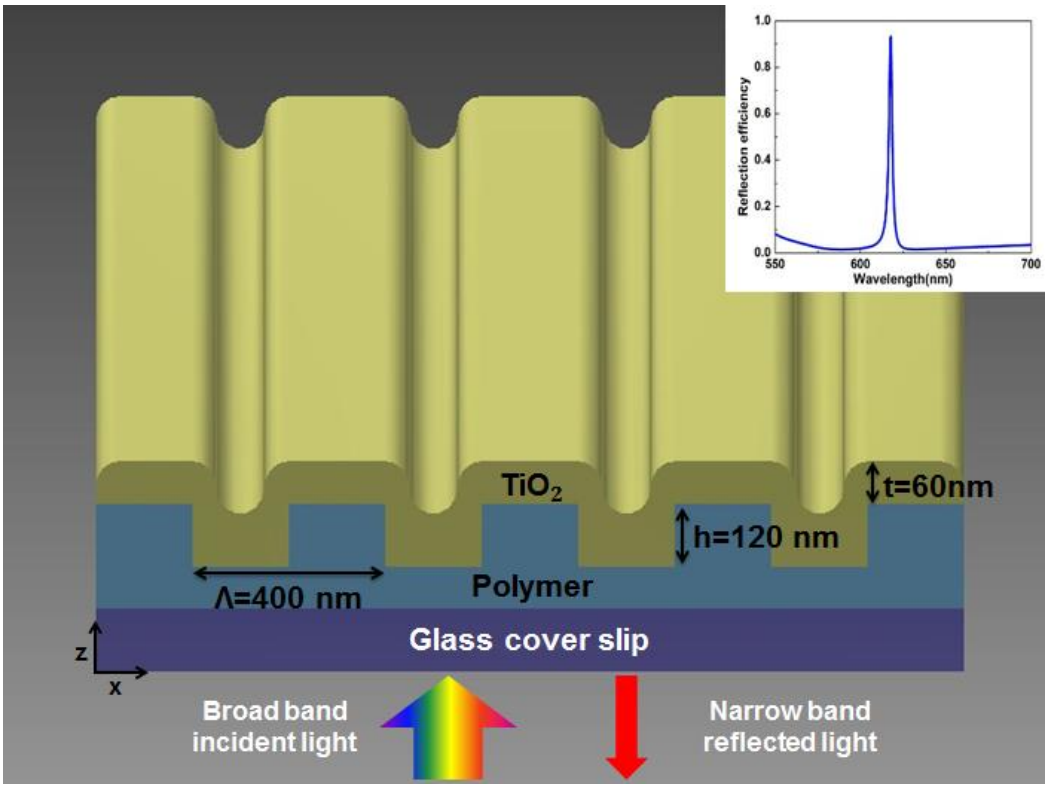


Figure 3 Schematic diagram of the photonic crystal (PC) biosensor. A PC sensor is comprised of a replica molded polymer grating overcoated with a high refractive index thin film of TiO2. Inset: simulated reflection spectrum of PC biosensor under the illumination of broadband light source.

# CHAPTER 2

# INSTRUMENTATION

## 2.1 Optical Instruments

As a multi-function imaging system, PCEM is designed to support both label-free and enhanced fluorescence cell imaging. A schematic diagram of the PCEM instrument is shown in Fig. 4. The system is built upon the body of a standard microscope (Carl Zeiss Axio Observer Z1), but in addition to ordinary bright field imaging, a second illumination path is provided from the back of the microscope. The two imaging modalities can be selected by either using or not using the gray color mirror shown in Fig. 4.

For the label-free imaging, a fiber-coupled broadband LED (Thorlabs M617F1, $600 < \lambda < 650$ nm) is selected to provide narrow-band and non-coherent light. The fiber output is collimated and filtered by a polarizing beamsplitter cube to illuminate the PC with light that is polarized with its electric field vector oriented perpendicular to the grating lines. The polarized beam is focused by a cylindrical lens (f = 200 mm) to form a linear beam at the back focal plane of the objective lens (10x, Zeiss). After passing through the objective lens, the orientation of the line-shaped beam is rotated to illuminate the PC from below at normal incidence. The reflected light is projected, via a side port of the inverted microscope and a zoom lens, onto a narrow slit aperture at the input of an imaging spectrometer. The width of the adjustable slit was set to 30 μm for the work

reported here. Using this method, reflected light is collected from a linear region of the PC surface, where the width of the imaged line, 1.2 μm, is determined by the width of the entrance slit of the imaging spectrometer and the magnification power of the objective lens. The system incorporates a grating-based spectrometer (Acton Research) with a 512 × 512 pixel CCD camera (Photometrics Cascade 512). The line of reflected light, containing the resonant biosensor signal, is diffracted by the grating within the spectrometer (300 lines/mm) to produce a spatially resolved spectrum for each point along the line. Therefore, each pixel across the line is converted to a resonant reflection spectrum, containing a narrow bandwidth ($\Delta\lambda \sim 4$ nm) reflectance peak from the PC. The Peak Wavelength Value (PWV) of each peak is determined by fitting the spectrum to a second-order polynomial function, and then mathematically determining the maximum wavelength of the function. By fitting all 512 spectra, in a process that takes 20 msec, a line comprised of 512 pixels is generated that represents one line of a PWV image of the PC surface. With an effective magnification of 26x, each pixel in the line represents a ~ 0.6 μm region of the PC surface and 512 such pixels cover a total width of ~300 μm. To generate a two-dimensional PWV image of the PC surface, a motorized stage (Applied Scientific Instruments, MS2000) translates the sensor along the axis perpendicular to the imaged line in increments of 0.6 μm/step. Using this technique, a series of lines are assembled into an image at a rate of 0.1 sec/line and the same area on the PC surface can be scanned repeatedly. Each image is comprised of 512 by n pixels, where n can be selected

during each scan session, and each pixel represents a $0.6 \times 0.6$ μm region of the PC surface. A biosensor experiment involves measuring shifts in PWV. A baseline PWV image is gathered before the introduction of cells, when the PC is uniformly covered by cell media, which is aligned and mathematically subtracted from subsequent PWV images gathered during and after cell attachment.

For enhanced fluorescence imaging, the second illumination path is provided from a semiconductor laser ($\lambda$ = 637 nm, AlGaAs) to excite the fluorescent dyes. The laser is coupled to a polarization maintaining fiber to provide a linearly polarized beam, which is later collimated by a condenser lens yielding a laser beam with a diameter of 6.7 mm. A half-wave plate is then used to adjust the electric field polarization to be perpendicular to the PC grating lines, thus ensuring TM mode illumination. The output beam is focused by the same cylindrical lens in label-free optical path to form a linear beam at the back focal plane of the objective lens via a 50/50 beamsplitter. After passing through the objective lens, the laser is focused along the direction parallel to the PC grating while remaining collimated in the direction perpendicular to the grating. The width of the illumination line is 6 μm, effectively minimizing the exposure of fluorophores in adjacent areas. The PC is still placed on the motorized sample stage that moves in a direction perpendicular to the illumination line during experiments to cover a targeted area on the PC surface. The emitted fluorescence is collected by the objective and projected, via a side port of the inverted microscope and a zoom lens onto the EM-CCD camera. An emission filter is

placed in front of the camera to block the laser light coming from the source, which passed only the fluorescence emission photons. In order to match the resonance condition of PC, an angle tuning capability is needed to adjust the incident angle of the laser light. For this purpose, an assembly including the end of the PM fiber, the collimator, the half waveplate and the cylindrical lens is mounted on a motorized translation stage (Zaber LSM-25) that shifts the incident light along the horizontal direction. The lateral position displacement ($\Delta d$) of the laser light focused at the back focal plane of the objective effectively leads to a change in the angle ($\Delta\theta$) of illumination for the PC surface given by equation: $\Delta\theta = \tan^{-1}(\Delta d/f)$. The incident angle can be controlled from $-10°$ to $+10°$ with an increment of $0.03°$ by translating the motorized stage over a distance of 6 mm with a step size 0.01 mm.

To construct a two-dimensional fluorescence image, the sample stage holding the PC translates along the axis perpendicular to the imaged line with an increment of 0.6 μm/step, while the camera gathers the fluorescence intensity of the center pixel line within the illuminated region at each step position. Using this technique, a series of lines is assembled into an image at a rate of 0.1 s/line to form the whole image. After completing a scan, the stage can return to its starting position to repeat the scan using a second incident angle. The pixel resolution along the scan direction is determined by the step increment (0.6 μm) and the pixel resolution in the other direction is also 0.6 μm, as determined by the camera resolution and effective optical magnification of the system. Each image is

comprised of 512 × 512 pixels covering a ~ 300 × 300 μm region on the PC surface.

## 2.2 Software Controller

The software controller for PCEM was written in C# programming language aiming to manage the entire microscope system including the camera, sample stage, computer and the linearly motorized stage for laser light source. After the user selects the type of image to output, this controller can automatically complete the work of data acquisition, data processing and image generation. In the fluorescence imaging experiment, the controller is also able to tune the angle of the incident light by accurately controlling the position of the laser stage. An advantage of this controller over the previous versions of the PCEM instrument is that all the above functions are integrated into a single application program. Users do not need to open several different windows in each different step and reload the data again and again. The operation interface for this software is made up by six panels shown in Fig. 5.

The panel (a) is for camera setting. Based on the written drivers and provided API support for Hamamatsu EM-CCD, this panel is to able to initialize the camera according to the input settings, which include the integration time, EM gain, ADC gain and readout speed. When the camera is turned on, this panel keeps showing to the user the camera name and the current temperature obtained

from the camera. After the experiment is done, the user may click on “close camera” to stop the data acquisition.

Panel (b) can be used to either show the spectra when the spectrometer slit is narrow (~30 μm) or show the real-time bright field image when the spectrometer slit is wide open. After clicking on the “take spectrum” or “live camera” buttons, an extra window will pop out to image the light currently received by the camera. When the slit is narrow, the grating in spectrometer has a strong diffraction effect and the light is spectrally resolved, therefore the signal read by the camera is about light spectrum. The spectrum can be shown in the spectrum window (d) and the user can select whether to read only one single spectrum at the center position or the averaged spectrum of the whole areas. When the slit is wide, the grating works more as a reflector than a diffractor, thus the image shown in the pop-out window is a bright field image.

Panel (c) is the most important part of this software which is in charge of the scan process. Before each scan, the user selects the type of image to output. In the “Hyper spectrum type” list box, the user needs to choose “Peak wavelength value image”, “Peak intensity value image”, “Intensity image”, “Single wavelength image”. The “select wavelength” box is used to tell the computer the center wavelength of the collected light, and it should be the same value as the one set in spectrometer. The user also needs to set the step size and total number of scanned lines for the following scan. Usually the step size is set to be 6 kÅ (= 0.6 μm) to match the image resolution of the microscope and the number of

scanned lines is 512. After clicking on “scan data”, the controller will automatically move the sample stage back half the length of the total scan distance to start the scan. During each scan, the stage moves step-by-step while the camera reads the spectrum information at each step position. To generate the finally output image, the computer first reads the command input before with the image type. For the PWV image, the computer will record the wavelength value of the spectrum peak position as the pixel value through a peak fitting algorithms. The computer firstly roughly searches the highest intensity region in the spectrum and then fits the data into a second-order polynomial to accurately find the peak wavelength. For the peak intensity value (PIV) image, the computer does the same searching and fitting work but outputs the spectrum intensity of the peak position as the pixel value. For the intensity image, the spectrum intensity at all wavelength values is summed together as the pixel value at each point. For the single wavelength image, the system tracks the spectrum intensity change at only the selected wavelength value and takes such intensity as the output pixel value in a similar manner as the SPRi. To obtain a good spectrum signal, it is also necessary to take the reference spectrum, the reflection spectrum of light source without the presence of PC, and the dark spectrum, the spectrum signal receives by the system when light source is off. For the practical use of this software, we also add a long scan function to it. The user can set the time interval between each scan and the total number of scans. In this way, the PCEM controller can achieve

a long-time observation of the cells. All the data is automatically saved by this software.

Panel (d) is the window to show the reflection spectrum of light collected by the CCD camera.

Panel (e) controls the motion of the sample stage except the scan period. User can take a specific position (usually the corner position of the PC biosensor) as the reference point by clicking on “Reference point”. Then all the motion of the sample stage takes this position as the zero in coordinates. After selecting the scan area, the user can acquire the relative coordinates of the scan position to the reference point and record that coordinates. This can help the user to find exactly the position of last scan even after the user changes the stage position for other purposes. And if the user wants to take a multi-points long scan, a long scan that tracks the images at several different places, the coordinates of the desired scan position needs to be input and the “Multi points scan” checkbox needs to be checked.

Panel (f) is only for the enhanced fluorescence experiments. The “Talk”, “Open”, “Close” and “Ports” buttons are used to connect the computer with the motorized stage that holds the laser light source. For each enhanced fluorescence experiment, it is important to find the resonant incident angle of the PC sample, so the “Angle scan” button can travel the motorized stage from the “Start” position to the “End” position with the input “Step size” and record the average image intensity at each step position. During this period, information of the current

position and the current intensity value continuously shows up in the “Position” and the “Intensity” box. The position with maximum intensity is then recorded by the computer. After the angle scan, by clicking on “Get to resonance position”, the stage can moves to the position that matches the PC resonant conditions. Then by clicking on “Scan”, the system behaves almost the same as under the command “Scan data”, except the computer directly takes the pixel line with the highest fluorescence intensity value and generates the output images with those pixel lines.

## 2.3 Figures

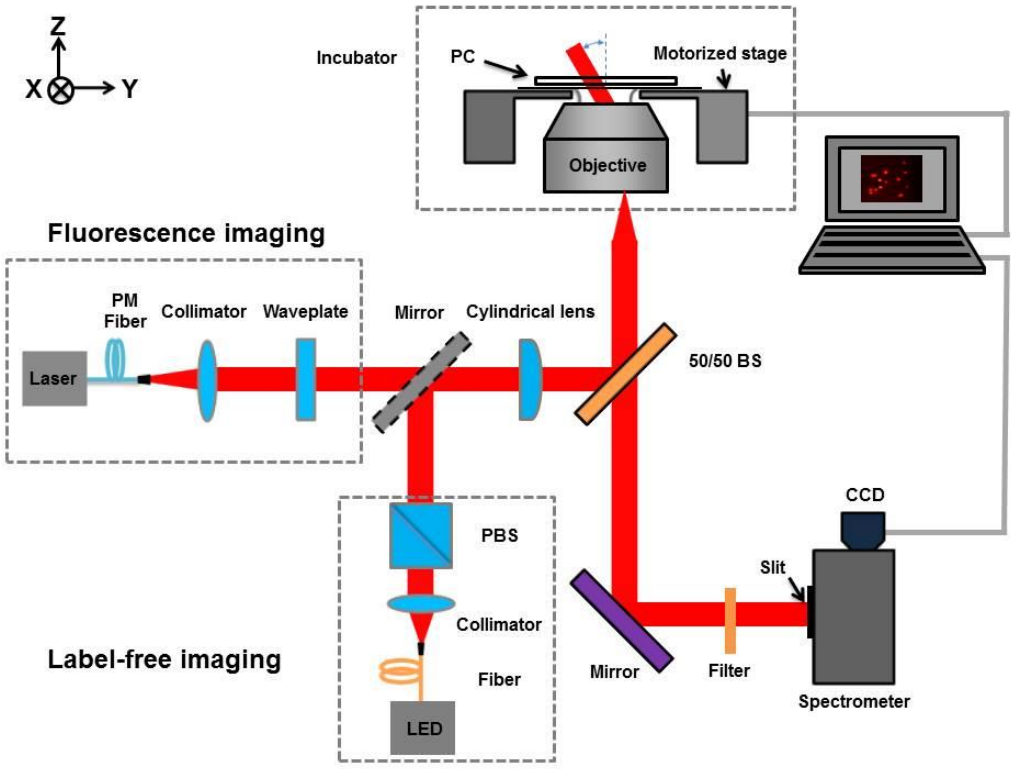


Figure 4 Instrument schematic of the PCEM. Illumination from a fiber-coupled LED is collimated and passed through a polarizing beamsplitter (PBS) to create a pure electric field polarization perpendicular to the PC grating. A cylindrical lens focuses the light to a line at the back focal plane of the objective. The PC resonantly reflects only a narrow band of wavelengths, which are collected through the entrance slit of an imaging spectrometer.

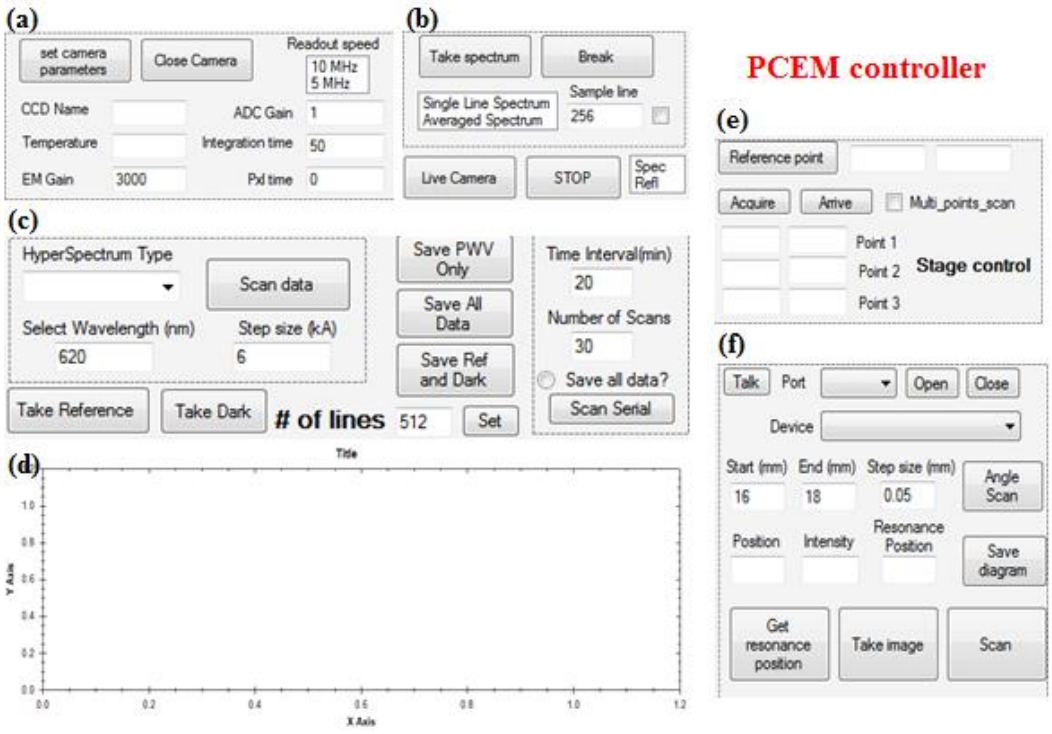


Figure 5 Operation interface of the PCEM software controller is made up of six panels: (a) camera setting, (b) spectrum setting, (c) scan setting, (d) spectrum read-out window, (e) sample stage setting, and (f) laser stage setting.

# CHAPTER 3

# LABEL-FREE IMAGING

## 3.1 Label-Free Cell Imaging

The most commonly used method for identification of differentiating stem cells is the labor- and time-intensive methylcellulose assay, which only reveals the identity of the colonies weeks after commitment occurs [24-26]. Furthermore, this approach requires cells to be resuspended in liquid phase, thereby altering many of the environmental cues that yielded the observed differential development. Using PCEM, it is possible to capture the dynamics of cell morphology and cell-matrix interactions during complex processes such as stem cell differentiation under real-time conditions (with less than 60 seconds between subsequent images). Such a tool would be critical for examining the potential of cell attachment signatures as a proxy for stem cell lineage commitment, particularly considering that such analyses could be performed without disturbing the extracellular environment.

As cells attach and spread, positive PWV shifts are observed due to an increase in the concentration of cellular material within the evanescent field region of the PC. A PWV image for human pancreatic cancer cells (Panc-1) is compared to a brightfield image of the same cells in Fig. 6. Morphological profiles are consistent with healthy, attachment-dependent cells. Representative spectra are shown from inside and outside the cell region, demonstrating a

definitive whole-spectrum shift of the characteristic resonant peak. Clearly visible boundaries of ~ 0.5 nm PWV shifts demonstrate the ability of PCEM to provide information about the geometry of attachment, which has been shown to have significant implications for both the classification of differentiating stem cells [27], and the metastatic potential of tumor cells [28]. In addition, sub-cellular variation of PWV is indicative not only of the presence of cellular adhesion, but also modulation in the strength of attachment. For example, cell "2" in Fig. 6 shows a gradient in cell attachment strength from left to right. A region of greater PWV shift along the leading edge suggests the formation of lamellipodia, indicating a higher concentration of intracellular matter than is present in the rest of the cellular attachment footprint. As it can be assumed that the majority of this lower-PWV shifted footprint occurs under regions of cytosol, the increased PWV of the cell boundary, especially in these protrusions, most likely can be attributed to the formation of actin bundles at sites of focal adhesion, a process thoroughly documented via traditional, yet cytotoxic, fluorescent staining techniques [29-31].

Next, murine dental stem cells (mHAT9a) were cultured and allowed to attach to a PC surface prepared with fibronectin over a period of two hours (shown in Fig. 7). From the series of PWV images gathered at 3 minute intervals, initial attachment times can be identified within the 3 minute period of image acquisition. Cells are observed attaching to the treated surface, with initial attachment characterized by small, round areas of PWV shift, consistent with spherical cells exiting suspension. As time progresses, average cell diameter

increases, and membrane boundaries become more irregular as cellular processes begin to extend from cell bodies. Many cells maintain highest shifts at their periphery, which is consistent with the high concentration of cytoskeletal protein necessary for boundary maintenance and lamellar extension. Random locomotion is observable, which reveals that cellular detachment results in a full recovery of initial PWV values when a cell moves to a new location. We observe no preference for the cells to extend themselves or to move along the direction of the PC grating.

Cellular apoptosis and detachment were also studied. Using another fibronectin-treated PC biosensor, mHAT9a cells were allowed to attach to the sensor surface for 3 hours. A final concentration of 2 μm staurosporine, shown to induce apoptosis via protein kinase inhibition [32, 33], was added to the cell chamber and mixed for 15 seconds. Cells were imaged every 20 minutes for 18 hours. Initial cells appear healthy, with various filopodia extending radially from cell bodies. As time progresses, the footprint of the cell bodies decreases, and several of the cells appear to detach completely. Other cells appear to undergo apoptosis prior to detachment, leaving behind remnants of cell membrane, which still produce a detectable PWV shift. The breakdown and modification of cell-cell and cell-ECM interactions is of great importance to answering questions about the progression of cancer cell detachment and metastasis from primary tumor sites. PCEM is unique in the fact that the biosensor response is a direct quantification and 2D localization of attachment at the single cell level, as opposed to indirect

methods of staining for actin bundle formation or even ensemble averaging of bulk dielectric properties. This direct observation available over a time scale of hours to days provides a natural tool for the future study of cancer cell detachment and metastasis.

We next sought to validate the use of PCEM imaging in examining cell-mediated chemotaxis (shown in Fig. 8). The importance of stromal cell-derived factor-1 (SDF-1α) in the directed chemotaxis of differentiating cells is well-known for a myriad of situations including hypoxic ocular neovascularization, capillary formation and adipocyte differentiation in human adipose tissue, and bone regeneration in traumatic brain injury [34-36]. More recently, SDF-1α and its effect in attracting CXCR4 receptor positive cells have been investigated in dental healing and regeneration. However, current mechanisms for studying the recruitment of dental stem cells have been based on fixing and staining cells [37, 38]. As the observed migration occurs on the order of days, label-based assays are not feasible for extended time course studies. PCEM provides an opportunity to monitor such events as they occur.

We examined mHAT9a chemotaxis in response to beads soaked in SDF-1α, a chemoattractant to which the receptor CXCR4 is sensitive [39]. After a bead was placed on the sensor surface, attached cells were observed to move in the direction of the eluting bead. Probing lamellipodia extend in multiple directions around the cell, but only projections formed in the direction of the bead are maintained by the migrating cells. Attachment in the trailing edge of the cell

decreases over time as the cell bodies proceed in the direction of chemotaxis, resulting in a return of the sensor to its native state. The experiment was repeated with a mHAT cell line with a constitutive knockout of the CXCR4 coding gene, and no directional movement was observed. This suggests that the observed cellular movement was indeed due to chemotaxis, as opposed to nonspecific locomotion. Critically, we do not observe preferential movement or extension of cell processes in the direction of the PC grating lines. To our knowledge, this represents the first label-free time-lapse imaging of the attachment localization of living cells during chemotaxis.

It has been shown that SDF-1α/CXCR4 mediated recruitment of dental stem cells is likely an important inflammatory response and underlying promoter of reparative dentin formation [40]. Further investigation of the SDF-1α/CXCR4 pathway with the PCEM technology could provide a valuable investigation of morphological changes induced by the inflammatory response of dental stem cells to dental damage.

### 3.2 Label-Free Nanoparticle Imaging

Nanoparticles (NP) prepared from dielectric, semiconductor, metal, and magnetic materials have recently become important elements of biosensor technology due to the ability to prepare their surfaces with ligands that enable them to recognize specific target molecules, and their ability to interact with electromagnetic fields in useful ways [41, 42]. For example, nanoparticles with

dielectric permittivity greater than that of water may be used as secondary tags for enhancing the signals from resonant optical biosensors [43], while magnetic nanoparticles are used to facilitate particle manipulation while at the same time providing a mass amplification tag for acoustic biosensors [44]. Likewise, metallic nanoparticles, comprised of silver or gold, couple with external illumination sources to generate surface plasmons, which are used to enhance local electric fields on the nanoparticle surface [45].

While many biosensing approaches are capable of sensing the adsorption of large numbers of nanoparticles [46], several approaches are capable of detecting the presence of a single nanoparticle, if the particle is adsorbed to a specific active location [47]. Due to the difficulty of directing analytes to precise locations on a substrate surface where a biosensor has sensitivity, one approach to overcoming this limitation is to utilize a biosensor surface in which the entire surface area is active as a sensor. Through the use of an imaging detection approach, the adsorption of analyte upon any region within the field of view may be measured. Imaging-based biodetection utilizing optical sensors has been demonstrated using surface plasmon resonance, photonic crystal biosensors, and dielectric thin film interference sensors. Such approaches are advantageous because analytes that produce highly localized changes in dielectric permittivity, such as cells, virus particles, or nanoparticles, may be detected, with the potential to observe the attachment of individual targets.

Here, we apply PCEM to imaging the attachment of dielectric and metallic nanoparticles upon a photonic crystal (PC) surface (Fig. 9). While our initial demonstration of PCEM described imaging the spatial distribution and time evolution of live cell attachment strength to a functionalized PC surface with 0.6 mm pixel resolution, here we report the detection of nanoparticles that are smaller than the pixel size. We demonstrate that metallic Au nanoparticles or nanorods produce highly localized effects upon the PC resonant reflection spectrum that enable individually attached particles to be easily observed by two distinct mechanisms, for particles as small as ~65 nm × 30 nm. We observe that the dielectric permittivity of particles results in a local shift in the resonant wavelength of the PC, while the optical absorption of nanoparticles results in a localized reduction in the resonant reflectivity magnitude. We anticipate the use of dielectric or metallic nanoparticles as functionalized tags in "sandwich" style assays that can be used to visualize the presence of individual captured analyte biomolecules upon a PC surface. PCEM nanoparticle imaging offers an attractive alternative to detection of fluorescent nanoparticles, as PCEM requires only low power broadband illumination, does not suffer from photobleaching, can provide long-term time-course data, and can be utilized for any type of nanoparticle tag.

## 3.3 Figures

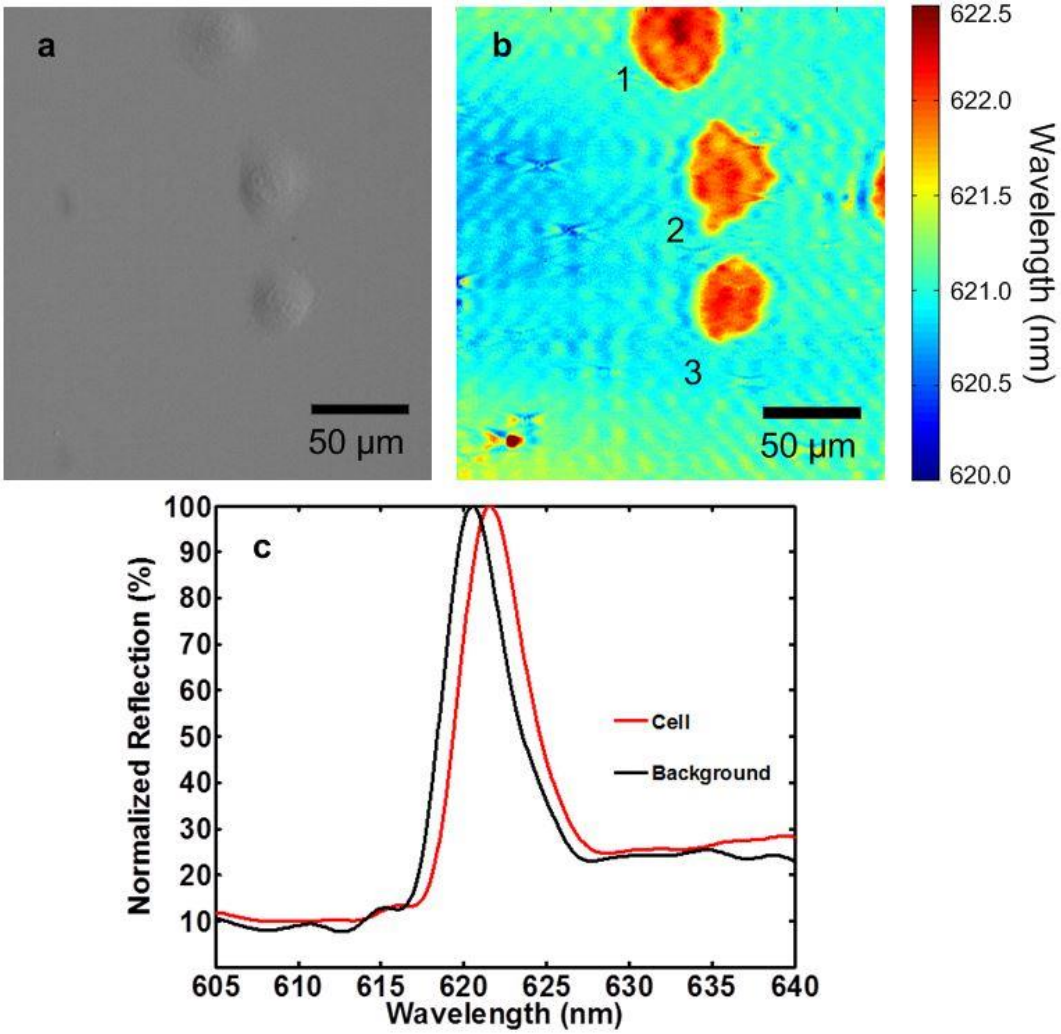


Figure 6 (a) Bright field and (b) PWV imaging of Panc-1 cells attached to the PC surface. Cells were seeded onto a fibronectin-coated sensor and allowed to incubate for 2 hours before imaging. Lamellipodial extensions are visible, especially from cell 2, demonstrating the ability of PCEM to resolve regional differences in single-cell attachment. Darker shading indicates regions of higher

protein concentration, and is present in regions near the boundary of lamellipodia formation, consistent with the creation of actin bundles. (c) Representative regions of cellular attachment. Selected areas of the PWV image from beneath a cell show the PWV shift of a typical Panc-1 cell is ~1.0 nm, and consistent throughout the entire spectrum at those locations.

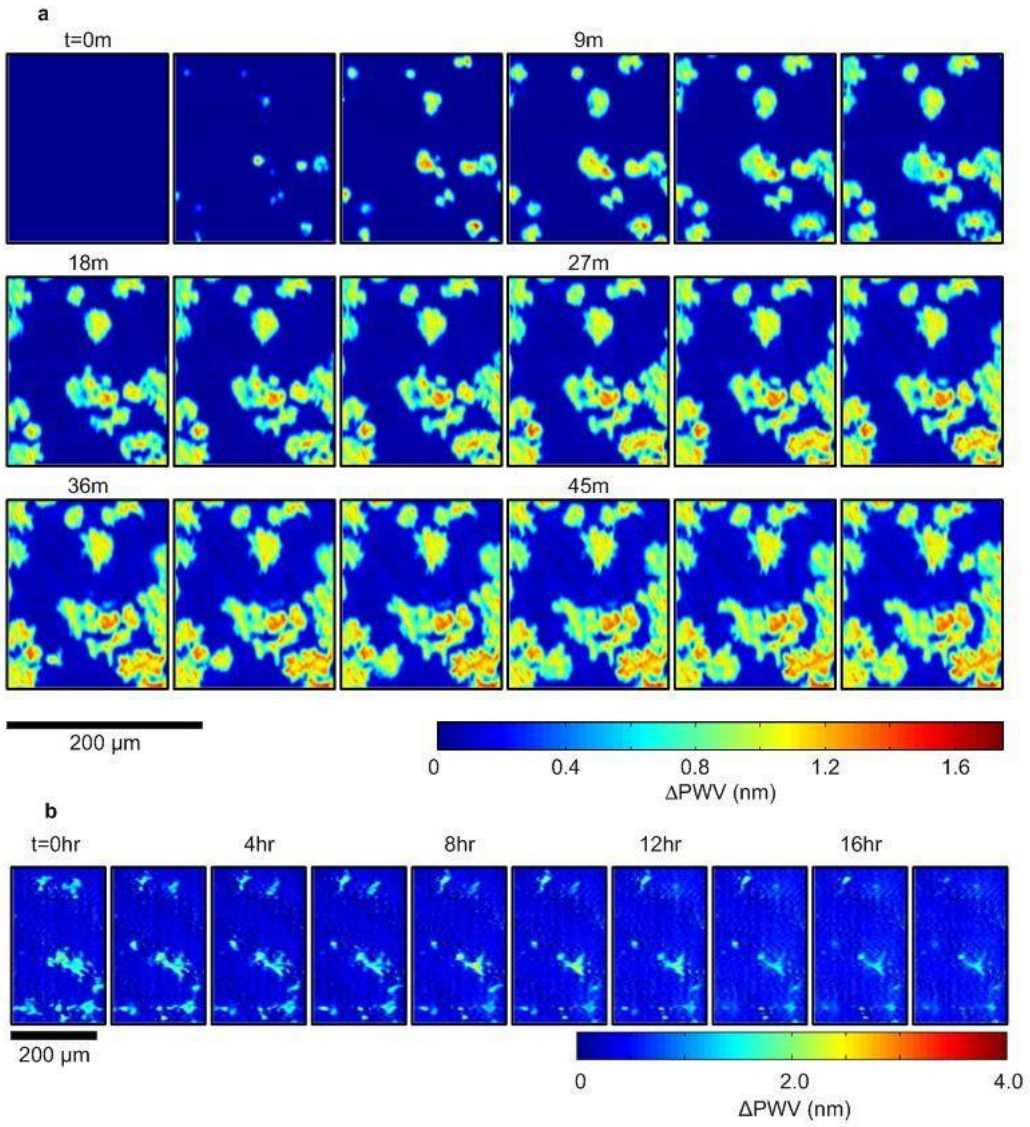


Figure 7 (a) Time lapse PWV images of cellular attachment of mHAT9a cells. Cells were seeded at 20,000 cells/ml on a fibronectin-coated sensor surface. After 3 minutes, regions of initial cell attachment appear as small, round regions, which are consistent with spheroid, trypsinized cells coming out of suspension and attaching to a surface. As time progresses, both the size of the cells and intensity

of the PWV shift induced by them increases, indicating a higher localization of cellular material at the sensor surface, which can be expected during cell spreading. Finally, once cells are sufficiently attached, cellular processes can be observed sensing the cells' microenvironment in all directions. The outer irregular boundaries of the cells have a relatively low PWV, consistent with thin, exploratory filopodia, accompanied by a more heavily attached region slightly immediately adjacent in the cell interior, likely a result of actin bundle formation. (b) Time lapse PWV images of mHAT9a apoptosis and detachment. Cells were seeded at 8,000 cells/ml onto a fibronectin-coated sensor surface. Cells that detach can be observed by the gradual retraction of filopodia and overall cell rounding before the PWV shift disappears entirely. Some cells appear to undergo apoptosis while still attached, leaving remnants of cell membranes and protein on the sensor surface. ΔPWV data was attained via background subtraction from an initial image taken before cell attachment (t = 0).

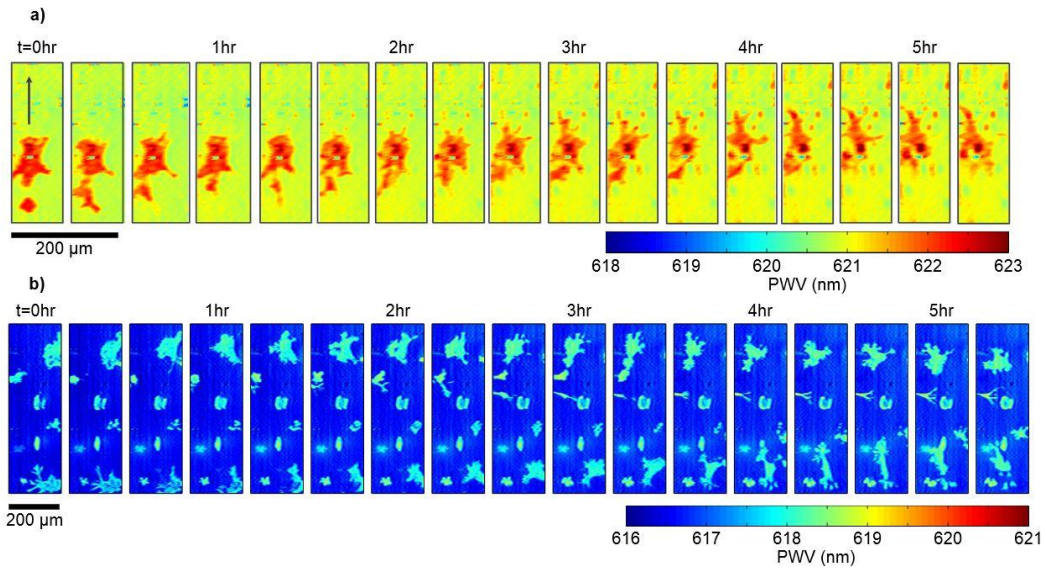


Figure 8 (a) Time lapse PWV images of chemotaxis of mHAT9a cells. Cells were deposited on the sensor surface at a concentration of 8,000 cells/ml and allowed to attach for 2 hours before imaging. An agarose bead was placed at a location approximately 100 microns above the top of the image, and PWV images were collected every 20 minutes after the bead was placed. Cell movement direction is indicated with an arrow in the leftmost frame. (b) CXCR4 knockout cells exhibit non-directional movement on the sensor surface. Similarly prepared, CXCR4 mutants do not show directional movement toward the bead, demonstrating that the previously observed directional locomotion was due to chemotaxis.

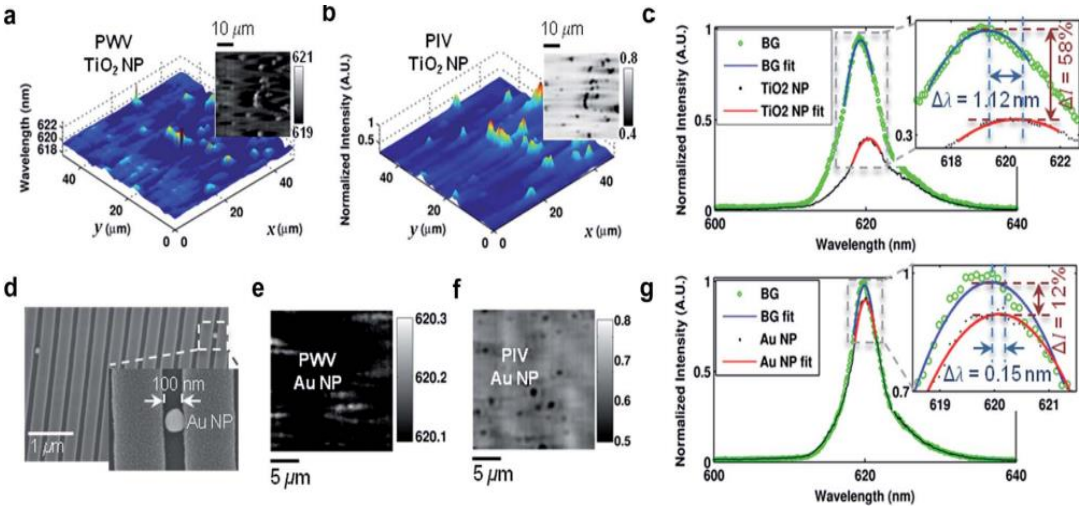


Figure 9 PCEM detection of randomly distributed TiO2 and Au nanoparticles (NP). (a) PCEM-detected PWV image of the $TiO_2$ NP displayed in a 3D surface plot. Inset: 2D PWV image in grayscale. (b) PCEM detected PIV image of the $TiO_2$ NP displayed in a 3D surface plot (inversed for comparison). Inset: 2D PIV image in gray scale. (c) Normalized spectrum of a 500 nm $TiO_2$ NP and a background pixel. Inset: Zoomed in image of the normalized spectrum with 2D polynomial fitting ($TiO_2$ NP fitting in red line, background fitting in blue line), indicating a PWV shift of $\Delta\lambda$ = 1.12 nm and a PIV reduction of $\Delta I$ = 58% when the NP is present. (d) Scanning electron micrograph of the Au NP on PC surface. Inset: Zoomed in image. PCEM detected (e) PWV image and (f) PIV image of the Au NP displayed in 2D with gray scale. (g) Normalized spectrum of a 100 nm Au NP and a background pixel. Inset: zoomed in image of the normalized spectrum with 2D polynomial fitting (Au NP fitting in red line, background fitting in blue line), indicating a PWV shift of $\Delta\lambda$ = 0.15 nm and a PIV reduction of $\Delta I$ = 12% when the NP is present.

# CHAPTER 4

## ENHANCED-FLUORESCENCE IMAGING

Several available approaches for visualization of cell-substrate interactions utilize fluorescent dyes that label specifically targeted cell structures, and fluorescent excitation methods that concentrate illumination energy to a confined zone on a transparent glass substrate or waveguide that is in direct contact with adherent cells. For example, total internal reflection fluorescence (TIRF) microscopy can selectively excite fluorophores near the adherent cell surface, while minimizing the fluorescence signal originating from the bulk of the cell [9] through a spatially restricted evanescent field upon a substrate surface when total internal reflection occurs. While TIRF microscopy has been broadly adopted through the availability of specialized microscope objectives, the approach is not able to differentiate between a locus of high fluorescence intensity that is bright because it is close to the cell-substrate interface, and a high intensity region of an image that is bright because it contains a high concentration of fluorescent dye. Confocal microscopy is another important technique that is used to visualize features of cell membranes, in which a diffraction-limited focal volume of laser illumination is scanned through the three-dimensional volume of the cell. Although confocal microscopy can specifically target volume elements of the cell that are close to the boundary with the surface, the approach also results in background excitation of components that are above/below the region of greatest

illumination intensity that belong to the cell body. Further, the throughput of confocal microscopy for rapidly imaging many cells in a large field of view is limited by the necessity of scanning the focused spot [48].

In order to address the limitations of TIRF and confocal microscopy, there has been intense interest in the development of surfaces and nanostructures that can more effectively couple light from a fluorescence excitation source, and spatially confine it to the region of a cell that adheres to the surface. These techniques can be advantageous because they can effectively amplify the excitation intensity beyond that available from an ordinary glass surface, resulting in greater fluorescent intensity than would be available from TIRF, given an identical illumination intensity.

While the first demonstrations of enhanced fluorescence appeared shortly after the discovery of surface enhanced Raman scattering almost three decades ago [49-51], the application of this method to improving bioassays has only occurred recently, in conjunction with the increased use of fluorescence protocols in life sciences research. Enhancing fluorescence typically relies on an interaction between a fluorophore and a resonant optical structure, the most common of which are metal nanoparticles, smooth metal surfaces, and nanostructure metal surfaces that support plasmon resonances. These resonances can affect fluorophores in a variety of ways: they can amplify excitation light [52], alter the spatial distribution of the fluorophore emission [53], modify the radiative lifetime of the fluorophore [54], or simultaneously perform more than one of these

functions [55-57]. Metal nanostructures have been demonstrated to enhance fluorescence for applications such as immunoassays [58] and cell imaging [59]. Previous demonstrations of metal-induced fluorescence enhancement have shown a signal increase of more than one order of magnitude [60, 61]. However, fluorophores in close proximity to metals (within 10 nm) often transfer their energy non-radiatively as well [62]. Fluorescence enhancement using metal surfaces or metal nanoparticles suffers from quenching if the fluorophore is too close to the metal, while electromagnetic fields associated with localized surface plasmons decay rapidly with distance as one moves away from the metal, resulting in very stringent requirements for surface-fluorophore spacing [63]. The low quality-factor of metal-based resonances, due to optical absorption, further reduces the achievable amplification factor for metal-enhanced fluorescence [64, 65].

Photonic crystals (PCs), or periodic arrangements of materials with differing dielectric constants, represent a powerful class of substrates for enhancing fluorescence. The PCs used in our research are comprised of a periodically modulated low refractive index polymer surface structure coated with a high refractive index dielectric layer of $TiO_2$, and capped with a low refractive index thin film of $SiO_2$ in which the period is smaller than the wavelength of light used to excite the structure (Fig. 10a). A resonance in this structure is excited when evanescent diffracted orders couple to modes of an effective high refractive index layer, and are re-radiated through diffraction in-phase with the reflected

zeroth-order wave and out-of-phase with the transmitted zeroth-order wave [21]. The dispersion of the PC then reveals these resonances as transmission dips (Fig. 10d) upon white light illumination, resulting from the coupling of light at specific incidence angles and wavelengths to the structure. These resonances are capable of enhancing fluorescence in a similar fashion to surface plasmon resonances, taking advantage of two phenomena: *enhanced excitation* and *enhanced extraction*. Enhanced excitation is the result of incident radiation coupling to a PC resonance, which increases the local electric field intensity throughout the structure. These fields decay exponentially as one moves way from the substrate surface (Fig. 10e and 10f), in a similar fashion to TIRF microscopy, but the resonance coupling provides a constructive interference effect that amplifies the incident wave [66]. Thus enhanced excitation provides the benefit of localized surface-bound fluorophore excitation observed with TIRF, but with increased performance due to field enhancement. Multiplied with this enhancement effect is enhanced extraction, whereby fluorophore emission couples to the PC and is redirected along the PC dispersion [67]. This mechanism helps to claim emitted light that otherwise may have been lost to guided modes within the substrate or to emission at oblique angles not collected by the detection optics. Enhanced extraction increases the percentage of fluorescence emission that is available for detection. Overall, photonic crystal enhanced fluorescence (PCEF) provides an optically active surface capable of providing uniform fluorescence enhancement

over large areas without the quenching effects that limit metal enhanced fluorescence approaches.

PCEF offers an additional unique feature that is not available in TIRF microscopy. For effective fluorescence enhancement by PCEF, the illumination angle of a monochromatic light source must be chosen to couple efficiently with the resonant mode used for enhanced excitation [68] by matching the illumination angle with the resonant coupling angle of the PC. However, by intentional adjustment of the incident angle to an off-resonant condition, one may obtain "ordinary" laser illumination, and thus it is simple to adjust the illumination between an "on-resonant" and an "off-resonant" state, effectively switching the enhancement effect on/off at will. In this thesis, we take advantage of this capability to create spatial maps of the PCEF enhancement factor of fluorescence-emitting regions on the surface and inside live cells. Rather than generating images of florescence intensity, as performed by TIRF, that result in fluorescence intensities that are dependent upon both the local dye concentration and the position of the emitters with respect to the substrate surface, PCEF microscopy creates fluorescence enhancement factor images, that derive their magnitude only from the proximity of the fluorescent emitter from the surface (Fig. 10f). While previous publications have described the application of PCEF in the context of microarrays of biomolecular assays for multiplexed detection of soluble protein biomarkers [69], gene expression [20], and miRNA [70], this work represents the first report of PCEF for fluorescence imaging of cells, in which alternating on/off-

resonance images are used to derive maps of the surface engagement of cell structures. Using dyes that target either outer cell membrane components or internal (nucleus) components of cells, we demonstrate that PCEF microscopy is capable of providing information about the spatial distribution of cell-surface interactions at the single-cell level that is not available from existing forms of microscopy, and that the approach is amenable to large fields of view, without the need for coupling prisms, coupling fluids, or special microscope objectives.

## 4.1 Enhancement Characterization

To characterize the resonant response of PC under the illumination of a TM polarized laser, a commercially available electromagnetic simulation package (FDTD Solutions, Lumerical Inc.) was used to study the optical field distribution (normalized to incident intensity) and the distance dependence of the enhancement effect. Since the fluorophores interact with excitation light primarily through excitation of their internal electrons, only electric field components are considered. One period of the PC structure was studied with a periodic boundary condition applied along the direction perpendicular to the grating lines, as shown in Fig. 10e.

To simulate the electric field associated with the PC biosensor used in real experiments, the corners of grating were slightly rounded to match the shape observed via AFM, and the superstrate material was chosen to represent water ($n_{water}$ = 1.33). The illumination is provided by a monochromatic plane wave

light source at a wavelength $\lambda$ = 637 nm, (the same wavelength used for experiments) and a magnitude, represented by the power of the incident electric field of $|E|^2 = 1\ (V/m)^2$. In our simulation, the on-resonance incident angle for a wavelength of $\lambda$ = 637 nm is designed to be $0°$ (normal incidence). Figure 10e (left) shows the spatial distribution of the near-field electric field at the resonance condition. The resonant electromagnetic standing wave generates surface-confined electric field power with magnitudes as high as $|E|^2$ = 100-300 $(V/m)^2$ in proximity to the $TiO_2$ layer with the evanescent tails penetrating both the substrate and superstrate materials. To demonstrate the difference between the on-resonance and the off-resonance condition, a second simulation was performed for the identical device structure and illumination source, but incident at an off-resonant coupling angle $5°$ from normal. As shown in Fig. 10e (right), the enhancement effect is generally eliminated due to the mismatch of incidence angle with the resonant coupling angle and the near-field electric field intensity is very close to $|E|^2 = 1\ (V/m)^2$. The distance dependence of the enhancement factor was estimated through simulation. The enhancement factor at a particular height was calculated as the ratio between the averaged electric field intensity at on- and off-resonance conditions, and is plotted as a function of the distance above the PC surface ranging from 2 nm to 600 nm, as shown by Fig. 10f. As expected, the enhancement effect decays exponentially as the fluorescent emitter is translated vertically from the PC surface, with the enhancement effect nearly completely eliminated for distances from the surface greater than 500 nm. Importantly, the

enhancement factor at each vertical distance is unique, suggesting that we can estimate the distance between a fluorescent emitter and the PC surface by measuring the fluorescence intensity at both on- and off-resonance and calculating the enhancement factor.

## 4.2 Enhanced-Fluorescence Cell Imaging

In order to characterize the adhesion properties of live cells and demonstrate the enhanced fluorescence imaging capability of PCEM, 3T3 fibroblast cells were cultured and observed when they are adherent to fiberonectin-treated PC sensors. Fibroblasts are the most common resident cells in the connective tissue. On injury, the fibroblast cells nearby the wound proliferate and produce large amounts of collagenous matrix to help to isolate and repair the damaged tissue [71]. The cell line was selected for initial demonstration of the PCEF microscopy due to their broad utility in tissue engineering and clinical applications.

The 3T3 fibroblasts (ATCC) were cultured in DMEM media with 5% fetal bovine serum. Silicone rubber gaskets (prepared using polydimethylsiloxane (PDMS)) gaskets were added to the sensor surface to provide a liquid container for cell attachment (1 mL volume). Prepared slides were treated with oxygen plasma, and incubated with 10 μg/mL fibronectin to encourage cellular attachment. Cells were incubated on the PC surface for 12 hours prior to labeling with fluorescent dyes. For membrane staining, a non-lectin, amphipathic

membrane dye that fluoresces at a wavelength of λ = 666 nm (Life Technologies, excitation/emission: 659/674 nm) was added at 1x concentration to the chamber and incubated for 10 minutes. Afterward, the chamber was rinsed with DMEM culture media. For nuclear staining, a cell-permanent nuclear stain that binds to DNA and fluoresces at λ = 647 nm (Life Technologies, excitation/emission 638/686 nm) was added to the chamber, and incubated for 30 minutes before imaging. Imaging was completed on the instrument as described above inside an environmentally controlled incubation chamber (Zeiss) maintaining constant 37 ℃ temperature and 5% $CO_2$.

When illuminated with the λ = 637 nm laser, the excitation efficiency for the nuclear dye is nearly 100%, but for the membrane dye, the excitation efficiency is expected to be only ~50%. Before each scan, an angle reflection spectrum is obtained, as shown in Fig. 11 (top left), to identify the on-and off-resonance incident angles. The experimental on-resonance incident angle is ±1.14 degrees. The two peaks observed in the spectrum are the result of bilateral symmetry of PC along the grating lines, which means that the incident angle can be equivalently coupled into the resonance mode from two symmetrical angles. To fully demonstrate the fluorescence enhancement ability of the PC, the off-resonance scan is always completed first, followed by an on-resonance scan of the same field of view, so photobleaching effects do not artificially inflate the observed enhancement factor. Other than the angle of incidence, all other

instrument settings were maintained between subsequent imaging sessions of a field of view.

i) Fluorescence imaging of cell membrane

Figure 3a shows the brightfield image of 3T3 fibroblasts incubated on a PC biosensor, showing a morphology that is consistent with surface-attached cells. The filopodia are easily visualized as they extend radially from the cell bodies confirming a healthy and fully-spread status of the examined cells. The off-resonance fluorescence image of the labeled cell membranes was taken first (Fig. 11b), showing clear cell attachment patterns, that are consistent with the brightfield image. Immediately after the off-resonance scan, the incident angle of the excitation laser was tuned to be the resonant angle of the PC followed by an on-resonance scan of the same field of view, as shown in Fig. 11c. Through comparison of the two images, obvious fluorescence intensity enhancement is obtained via resonant illumination of the PC surface. To quantify the intensity amplification effect at each pixel position, an enhancement factor image was generated by dividing the on-resonance net intensity by the off-resonance net intensity (Fig. 11d). A fivefold enhancement was achieved through the effect of only enhanced excitation, as indicated by the image colorbar.

Important information about cell adhesion can be inferred from the enhancement factor image. Due to the distance dependence characteristics of the resonant electric field strength shown by the previous simulation, the unequal excitation efficiency of fluorophores results from their difference in the vertical

distance from the PC surface. The higher enhancement factor exhibited by a fluorophore, the smaller gap exists between the fluorophore-bound cell component and its substrate. Consequently, the variation of the enhancement factor over intracellular locations not only implies the existence of cell binding to surface, but also evaluates the strength and gradient of the formed adhesion bonds. A three-dimensional plot of the enhancement factor (Fig. 11(e)) sketch the contours of the spatial profiles of the cell membrane that contacts the PC surface.

ii) Fluorescence imaging of cell nucleus

To extend the generality of PC enhanced fluorescence, we performed another live cell experiment with labeled nuclei. The brightfield, on-resonance, off-resonance and enhancement factor images are shown in Fig. 11(f)-(j). In contrast to the expected irregular morphological fluorescence patterns stemming from cell membrane shapes, the labeled nuclei appear to be circular, as expected. When the incident angle is on-resonance, cell nuclei in the evanescent field region show an enhancement factor as large as 20 times that of the off-resonance image. According to the simulated enhancement decay curve (Fig. 10(f)), we can estimate that nucleus-bound fluorophore is within 150 nm of the PC surface.

## 4.3 Figures

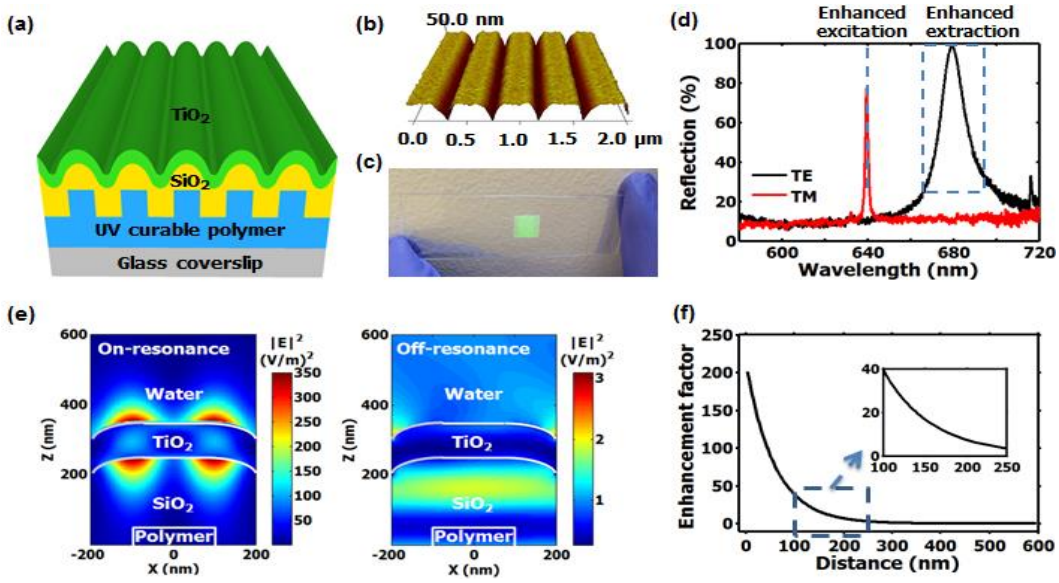


Figure 10 (a) Schematic diagram of the PC biosensor. (b) AFM image of the PC biosensor surface showing the grating period of 400 nm and grating depth of 50 nm. (c) Photograph of the PC biosensor on a standard microscope slide substrate. (d) Reflection spectrum of a PC biosensor. Red curve and black curve indicate the reflection response of PC under the illumination of TM polarized light and TE polarized light respectively. (e) FDTD simulation of evanescent electric field distribution when the PC biosensor is under resonant (left) and non-resonant (right) illumination. The electrical field intensity under on-resonance condition is enhanced maximally 350 times compared to the incident light intensity, while the off-resonance electrical field exhibits little intensity increase. (f) The distance dependence of the enhancement factor.

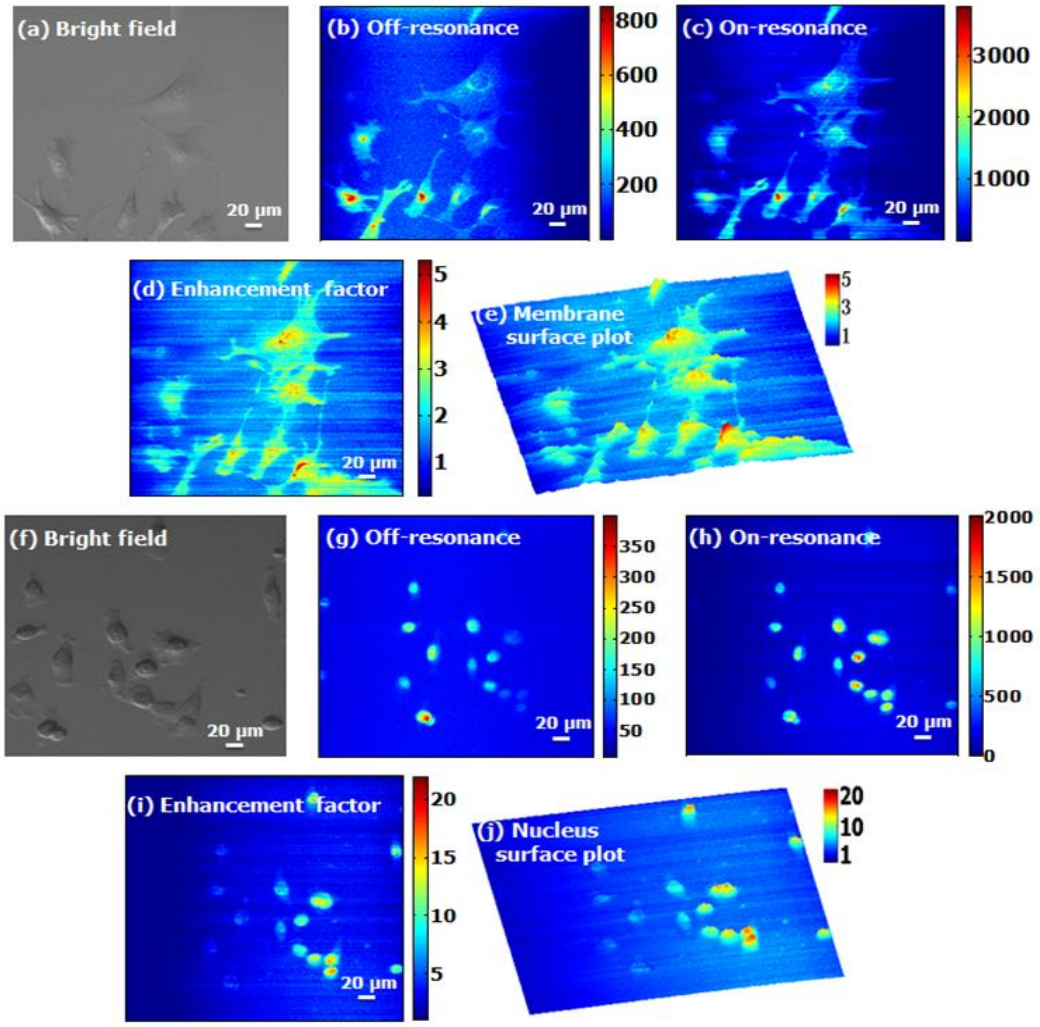


Figure 11 The (a) bright field, (b) off-resonance, (c) on-resonance, (d) enhancement factor, (e) 3D surface plot imaging of 3T3 cell membrane. Cells are labeled with plasma membrane dye with an excitation and emission wavelength at 659 nm and 674 nm respectively. And the (f) bright field, (g) off-resonance, (h) on-resonance, (i) enhancement factor, (j) 3D surface plot imaging of 3T3 cell nucleus. The cell nucleus dye is excited with a maximum at 638 nm when bound to DNA, with an emission maximum at 686 nm.

# CHAPTER 5

## CONCLUSION

PCEM represents a new imaging modality that can be easily integrated with a conventional optical microscope to enable quantified, near real-time, high resolution imaging of cell-surface interactions. While traditional microscopy techniques such as phase-contrast and DIC provide basic information about cellular morphology and general appearance, PCEM provides information that is specific to the interface between the cell and its substrate. By virtue of the surface-confined resonant electric field of the photonic crystal, PCEM enables high contrast imaging of the interaction strength of cells with a surface, providing a specific attachment footprint as opposed to a generalized shape of the entire three-dimensional cell body. The approach utilizes low cost illumination source from below, using a PC sensor structure that can be incorporated into standard coverslips (as demonstrated here), microscope slides, or microtiter plates that are typically used for cell research. PCEM clearly demonstrates that cell-surface attachment strength is not uniformly distributed within a cell or static as a function of time, but instead contains rich dynamic information that includes the rate of cell boundary extension, the size of a cell "footprint" on a surface, and the effect of the extracellular environment (including chemotactic gradients) on cell attachment.

The cell imaging experiments used to demonstrate PCEM were selected to

show that the spatial resolution of the approach is sufficient for clearly observing features such as spatial gradients in cell-surface attachment and the extension of fine-structured filopodia, attributes that are typically observed only using dyes or stains. As a label-free and enhanced-fluorescence detection approach, PCEM enables continuous monitoring of these phenomena over extended time periods that are compatible with the biological time scales of chemotaxis, apoptosis, differentiation, and proliferation. This thesis demonstrates, to our knowledge, the first time-lapse movies of cell-surface interaction monitoring at these time scales.

It is already well established that both the comparison of cancerous/non-cancerous cells and of cell lineages differentiated from pluripotent stem cells lend themselves to investigation via their unique morphologies and cellular attachment protein expression, with the majority of such differences easily visible via traditional microscopy. With PCEM, cellular attachment morphology can be directly observed, and attachment "profiles" for different cell types can be developed. By limiting the study of cell morphology to the specific density of cellular material present in the evanescent field region of a photonic crystal, attachment can be observed in a more direct method with less subjectivity than simple qualitative observation using traditional microscopy methods.

There is an increasing awareness of the importance of cellular adhesion and the mechanical microenvironment of cells on their behavior, yet directly measuring these attributes in a non-invasive fashion has proved difficult. PCEM provides a novel, robust methodology for the investigation of these attributes in a

controlled environment without chemical alteration. The relationship between mechanical microenvironmental cues and cancer cell behavior has been demonstrated, contributing significantly to tissue dysplasia and metastatic detachment [72]. With PCEM, it will be possible to investigate important components within the progression of tumor-development, such as the recruitment and movement of neutrophils to the cancer microenvironment. Neutrophil polarization and chemotaxis represent a challenging process to study as it presents a complex and dynamic set of cellular-ECM interactions. Near real-time imaging would allow for rapid improvement in our understanding of this and the other biological applications discussed herein, providing dynamic attachment information that is not currently available.

## REFERENCES


[1] G. Pattabiraman, E. A. Lidstone, K. Palasiewicz, B. T. Cunningham, and D. S. Ucker, "Recognition of apoptotic cells by viable cells is specific, ubiquitous, and species independent: Analysis using photonic crystal biosensors," *Molecular Biology of the Cell,* vol. 25, pp. 1704-1714, 2014.

[2] J. El-Ali, P. K. Sorger, and K. F. Jensen, "Cells on chips," *Nature,* vol. 442, pp. 403-411, Jul 27 2006.

[3] M. Barczyk, S. Carracedo, and D. Gullberg, "Integrins," *Cell and Tissue Research,* vol. 339, pp. 269-280, Jan 2010.

[4] B. M. Gumbiner, "Cell adhesion: The molecular basis of tissue architecture and morphogenesis," *Cell,* vol. 84, pp. 345-357, Feb 9 1996.

[5] "Milestones in light microscopy," *Nature Cell Biology,* vol. 11, pp. 1165-1165, Oct 2009.

[6] M. G. L. Gustafsson, "Surpassing the lateral resolution limit by a factor of two using structured illumination microscopy," *Journal of Microscopy-Oxford,* vol. 198, pp. 82-87, May 2000.

[7] J. W. Lichtman and J. A. Conchello, "Fluorescence microscopy," *Nature Methods,* vol. 2, pp. 910-919, Dec 2005.

[8] A. Piruska, I. Nikcevic, S. H. Lee, C. Ahn, W. R. Heineman, P. A. Limbach, and C. J. Seliskar, "The autofluorescence of plastic materials and chips measured under laser irradiation," *Lab on a Chip,* vol. 5, pp. 1348-1354, 2005.

[9] D. Axelrod, "Total internal reflection fluorescence microscopy in cell biology," *Traffic,* vol. 2, pp. 764-774, Nov 2001.

[10] A. L. Mattheyses, S. M. Simon, and J. Z. Rappoport, "Imaging with total internal reflection fluorescence microscopy for the cell biologist," *Journal of Cell Science,* vol. 123, pp. 3621-3628, 2010.

[11] M. M. A. Jamil, M. C. T. Denyer, M. Youseffi, S. T. Britland, S. Liu, C. W. See, M. G. Somekh, and J. Zhang, "Imaging of the cell surface interface using objective coupled widefield surface plasmon microscopy," *Journal of Structural Biology,* vol. 164, pp. 75-80, Oct 2008.

[12] A. W. Peterson, M. Halter, A. Tona, K. Bhadriraju, and A. L. Plant, "Surface plasmon resonance imaging of cells and surface-associated fibronectin," *BMC Cell Biology,* vol. 10, Feb 26 2009.

[13] B. Lin, P. Li, and B. T. Cunningham, "A label-free biosensor-based cell attachment assay for characterization of cell surface molecules," *Sensors and Actuators B-Chemical,* vol. 114, pp. 559-564, Apr 26 2006.

[14] B. Rothenhausler and W. Knoll, "Surface-plasmon microscopy," *Nature,* vol. 332, pp. 615-617, Apr 14 1988.

[15] M. E. Caldwell and E. M. Yeatman, "Surface-plasmon spatial light modulators based on liquid-crystal," *Applied Optics,* vol. 31, pp. 3880-3891, Jul 10 1992.

[16] M. Piliarik and J. Homola, "Surface plasmon resonance (SPR) sensors: Approaching their limits?," *Optics Express,* vol. 17, pp. 16505-16517, Sep 14 2009.

[17] I. D. Block, P. C. Mathias, N. Ganesh, S. I. Jones, B. R. Dorvel, V. Chaudhery, L. O. Vodkin, R. Bashir, and B. T. Cunningham, "A detection instrument for enhanced-fluorescence and label-free imaging on photonic crystal surfaces," *Optics Express,* vol. 17, pp. 13222-13235, Jul 20 2009.

[18] B. Cunningham, P. Li, B. Lin, and J. Pepper, "Colorimetric resonant reflection as a direct biochemical assay technique," *Sensors and Actuators B-Chemical,* vol. 81, pp. 316-328, Jan 5 2002.

[19] B. T. Cunningham, P. Li, S. Schulz, B. Lin, C. Baird, J. Gerstenmaier, C. Genick, F. Wang, E. Fine, and L. Laing, "Label-free assays on the BIND system," *Journal of Biomolecular Screening,* vol. 9, pp. 481-490, Sep 2004.

[20] P. C. Mathias, S. I. Jones, H. Y. Wu, F. Yang, N. Ganesh, D. O. Gonzalez, G. Bollero, L. O. Vodkin, and B. T. Cunningham, "Improved sensitivity of DNA microarrays using photonic crystal enhanced fluorescence," *Analytical Chemistry,* vol. 82, pp. 6854-6861, Aug 15 2010.

[21] D. Rosenblatt, A. Sharon, and A. A. Friesem, "Resonant grating waveguide structures," *IEEE Journal of Quantum Electronics,* vol. 33, pp. 2038-2059, Nov 1997.

[22] S. L. Reck-Peterson, N. D. Derr, and N. Stuurman, "Imaging single molecules using total internal reflection fluorescence microscopy (TIRFM)," *Cold Spring Harb Protoc*, vol. 3, pp. 1-11, March 2010.

[23] N. Blow, "Proteins and proteomics: Life on the surface," *Nature Methods*, vol. 6, pp. 389-392, May 2009.

[24] C. L. Miller and B. Lai, "Human and mouse hematopoietic colony-forming cell assays," in *Basic Cell Culture Protocols*, ed: Springer, 2005, pp. 71-89.

[25] N. I. zur Nieden, J. T. Cormier, D. E. Rancourt, and M. S. Kallos, "Embryonic stem cells remain highly pluripotent following long term expansion as aggregates in suspension bioreactors," *Journal of Biotechnology*, vol. 129, pp. 421-432, 5/1/ 2007.

[26] M. Winkler, N. Trieu, T. Feng, L. Jin, S. Walker, L. Singh, and H. T. Ku, "A quantitative assay for insulin-expressing colony-forming progenitors," *J Vis Exp*, p. e3148, 2011.

[27] K. A. Kilian, B. Bugarija, B. T. Lahn, and M. Mrksich, "Geometric cues for directing the differentiation of mesenchymal stem cells," *Proceedings of the National Academy of Sciences*, vol. 107, pp. 4872-4877, 2010.

[28] X. Tang, Q. Wen, T. B. Kuhlenschmidt, M. S. Kuhlenschmidt, P. A. Janmey, and T. A. Saif, "Attenuation of cell mechanosensitivity in colon cancer cells during in vitro metastasis," *PloS one*, vol. 7, p. e50443, 2012.

[29] B. Wehrle-Haller and B. A. Imhof, "Actin, microtubules and focal adhesion dynamics during cell migration," *The International Journal of Biochemistry & Cell Biology*, vol. 35, pp. 39-50, Jan 2003.

[30] G. Cooper, "Structure and organization of actin filaments," in *The Cell: A Molecular Approach*, G. Cooper, Ed., Sunderland, MA, 2004.

[31] J. T. Smith, J. T. Elkin, and W. M. Reichert, "Directed cell migration on fibronectin gradients: Effect of gradient slope," *Experimental Cell Research*, vol. 312, pp. 2424-2432, Aug 2006.

[32] B. S. Cummings, G. R. Kinsey, L. J. C. Bolchoz, and R. G. Schnellmann, "Identification of caspase-independent apoptosis in epithelial and cancer cells," *Journal of Pharmacology and Experimental Therapeutics*, vol. 310, pp. 126-134, July 1 2004.

[33] M. W. Karaman, S. Herrgard, D. K. Treiber, P. Gallant, C. E. Atteridge, B. T. Campbell, K. W. Chan, P. Ciceri, M. I. Davis, P. T. Edeen, R. Faraoni, M. Floyd, J. P. Hunt, D. J. Lockhart, Z. V. Milanov, M. J. Morrison, G. Pallares, H. K. Patel, S. Pritchard, L. M. Wodicka, and P. P. Zarrinkar, "A quantitative analysis of kinase inhibitor selectivity," *Nat Biotechnol,* vol. 26, pp. 127-32, 2008.

[34] R. L. e Silva, J. Shen, S. F. Hackett, S. Kachi, H. Akiyama, K. Kiuchi, K. Yokoi, M. C. Hatara, T. Lauer, and S. Aslam, "The SDF-1/CXCR4 ligand/receptor pair is an important contributor to several types of ocular neovascularization," *The FASEB Journal,* vol. 21, pp. 3219-3230, 2007.

[35] C. Sengenès, A. Miranville, M. Maumus, S. de Barros, R. Busse, and A. Bouloumié, "Chemotaxis and differentiation of human adipose tissue CD34+/CD31 − Progenitor cells: Role of stromal derived factor-1 released by adipose tissue capillary endothelial cells," *Stem Cells,* vol. 25, pp. 2269-2276, 2007.

[36] X. Liu, C. Zhou, Y. Li, Y. Ji, G. Xu, X. Wang, and J. Yan, "SDF-1 promotes endochondral bone repair during fracture healing at the traumatic brain injury condition," *PloS one,* vol. 8, p. e54077, 2013.

[37] L. Jiang, Y.-Q. Zhu, R. Du, Y.-X. Gu, L. Xia, F. Qin, and H. H. Ritchie, "The expression and role of stromal cell-derived factor-1alpha-CXCR4 axis in human dental pulp," *J Endod,* vol. 34, pp. 939-44, 2008.

[38] T. Suzuki, C. Lee, M. Chen, W. Zhao, S. Fu, J. Qi, G. Chotkowski, S. Eisig, A. Wong, and J. Mao, "Induced migration of dental pulp stem cells for in vivo pulp regeneration," *Journal of Dental Research,* vol. 90, pp. 1013-1018, 2011.

[39] M. Kucia, K. Jankowski, R. Reca, M. Wysoczynski, L. Bandura, D. J. Allendorf, J. Zhang, J. Ratajczak, and M. Z. Ratajczak, "CXCR4-SDF-1 signalling, locomotion, chemotaxis and adhesion," *J Mol Histol,* vol. 35, pp. 233-45, 2004.

[40] Q. M. Gong, J. J. Quan, H. W. Jiang, and J. Q. Ling, "Regulation of the stromal cell-derived factor-1alpha-CXCR4 axis in human dental pulp cells," *J Endod,* vol. 36, pp. 1499-503, Sep 2010.

[41] D. Ishii, K. Kinbara, Y. Ishida, N. Ishii, M. Okochi, M. Yohda, and T. Aida, "Chaperonin-mediated stabilization and ATP-triggered release of semiconductor nanoparticles," *Nature,* vol. 423, pp. 628-632, Jun 5 2003.

[42] K. T. Thurn, T. Paunesku, A. G. Wu, E. M. B. Brown, B. Lai, S. Vogt, J. Maser, M. Aslam, V. Dravid, R. Bergan, and G. E. Woloschak, "Labeling $TiO_2$ nanoparticles with dyes for optical fluorescence microscopy and determination of $TiO_2$-DNA nanoconjugate stability," *Small,* vol. 5, pp. 1318-1325, Jun 5 2009.

[43] R. C. Bailey, J. M. Nam, C. A. Mirkin, and J. T. Hupp, "Real-time multicolor DNA detection with chemoresponsive diffraction gratings and nanoparticle probes," *Journal of the American Chemical Society*, vol. 125, pp. 13541-13547, Nov 5 2003.

[44] M. F. Miller, B. P. Masters, and M. E. Lundstrom, "Method and apparatus for detection of analyte using a flexural plate wave device and magnetic particles," ed: Google Patents, 2007.

[45] Y. L. Wang, H. J. Chen, S. J. Dong, and E. K. Wang, "Surface-enhanced Raman scattering of silver-gold bimetallic nanostructures with hollow interiors," *Journal of Chemical Physics,* vol. 125, Jul 28 2006.

[46] J. Lee, W. J. Shen, K. Payer, T. P. Burg, and S. R. Manalis, "Toward attogram mass measurements in solution with suspended nanochannel resonators," *Nano Letters,* vol. 10, pp. 2537-2542, Jul 2010.

[47] J. G. Zhu, S. K. Ozdemir, Y. F. Xiao, L. Li, L. N. He, D. R. Chen, and L. Yang, "On-chip single nanoparticle detection and sizing by mode splitting in an ultrahigh-Q microresonator," *Nature Photonics,* vol. 4, pp. 122-122, Feb 2010.

[48] B. Joshi, S. S. Strugnell, J. G. Goetz, L. D. Kojic, M. E. Cox, O. L. Griffith, S. K. Chan, S. J. Jones, S. P. Leung, H. Masoudi, S. Leung, S. M. Wiseman, and I. R. Nabi, "Phosphorylated caveolin-1 regulates rho/ROCK-dependent focal adhesion dynamics and tumor cell migration and invasion," *Cancer Research,* vol. 68, pp. 8210-8220, Oct 15 2008.

[49] W. H. Weber and C. F. Eagen, "Energy transfer from an excited dye molecule to the surface plasmons of an adjacent metal," *Optics Letters,* vol. 4, pp. 236-238, 1979.

[50] A. M. Glass, P. F. Liao, J. G. Bergman, and D. H. Olson, "Interaction of metal particles with adsorbed dye molecules: Absorption and luminescence," *Optics Letters,* vol. 5, pp. 368-370, 1980.

[51] W. Knoll, M. R. Philpott, J. D. Swalen, and A. Girlando, "Emission of light from Ag metal gratings coated with dye monolayer assemblies," *Journal of Chemical Physics,* vol. 75, pp. 4795-4799, 1981.

[52] Y.-J. Hung, I. I. Smolyaninov, and C. C. Davis, "Fluorescence enhancement by surface gratings," *Optics Express,* vol. 14, pp. 10825-10830, 2006.

[53] I. Gryczynski, J. Malicka, Z. Gryczynski, and J. R. Lakowicz, "Radiative decay engineering 4. Experimental studies of surface plasmon-coupled directional emission," *Analytical Biochemistry,* vol. 324, pp. 170-182, 2004.

[54] O. L. Muskens, V. Giannini, J. A. Sanchez-Gil, and J. G. Rivas, "Strong enhancement of the radiative decay rate of emitters by single plasmonic nanoantennas," *Nano Letters,* vol. 7, pp. 2871-2875, 2007.

[55] J. R. Lakowicz, "Radiative decay engineering: biophysical and biomedical applications," *Analytical Biochemistry,* vol. 298, pp. 1-24, 2001.

[56] Y. Liu and S. Blair, "Fluorescence enhancement from an array of subwavelength metal apertures," *Optics Letters,* vol. 28, pp. 507-509, 2003.

[57] Y. Chen, K. Munechika, and D. S. Ginger, "Dependence of fluorescence intensity on the spectral overlap between fluorophores and plasmon resonant single silver nanoparticles," *Nano Letters,* vol. 7, pp. 690-696, 2007.

[58] J. Zhang, E. Matveeva, I. Gryczynski, Z. Leonenko, and J. R. Lakowicz, "Metal-Enhanced Fluoroimmunoassay on a silver film by vapor deposition," *Journal of Physical Chemistry B,* vol. 109, pp. 7969-7975, 2005.

[59] J. Zhang, Y. Fu, D. Liang, R. Y. Zhao, and J. R. Lakowicz, "Enhanced fluorescence images for labeled cells on silver island films," *Langmuir,* vol. 24, pp. 12542-12457, 2008.

[60] C. R. Sabanyagam and J. R. Lakowicz, "Increasing the sensitivity of DNA microarrays by metal-enahnced fluorescence using surface-bound silver nanoparticles," *Nucleic Acids Research,* vol. 35, p. e13, 2007.

[61] E. L. Moal, S. Leveque-Fort, M.-C. Potier, and E. Fort, "Nanoroughened plasmonic films for enhanced biosensing detection," *Nanotechnology,* vol. 20, p. 225502, 2009.

[62] I. Pockrand, A. Brillante, and D. Mobius, "Nonradiative decay of excited molecules near a metal surface," *Chemical Physics Letters,* vol. 69, pp. 499-504, 1980.

[63] J. Zhang, Y. Fu, M. H. Chowdhury, and J. R. Lakowicz, "Metal-enhanced signle-molecule fluorescence on silver particle monomer and dimer: Coupling effect between metal particles," *Nano Letters,* vol. 7, pp. 2101-2107, 2007.

[64] T. Hayakawa, S. T. Selvan, and M. Nogami, "Field enhancement effect of small Ag particles on teh fluorescence from Eu(3+)-doped $SiO_2$ glass," *Applied Physics Letters,* vol. 74, pp. 1513-1515, 1999.

[65] S. T. Selvan, T. Hayakawa, and M. Nogami, "Remarkable influence of silver islands on the enhancement of fluorescence from Eu(3+) ion-doped silica gels," *J. Phys. Chem. B,* vol. 103, pp. 7064-7067, 1999.

[66] N. Ganesh, P. C. Mathias, W. Zhang, and B. T. Cunningham, "Distance dependence of fluorescence enhancement from photonic crystal surfaces," *Journal of Applied Physics,* vol. 103, p. 083104, 2008.

[67] N. Ganesh, I. D. Block, P. C. Mathias, W. Zhang, E. Chow, V. Malyarchuk, and B. T. Cunningham, "Leaky-mode assisted fluorescence extraction: application to fluorescence enhancement biosensors," *Optics Express,* vol. 16, pp. 21626-21640, 2008.

[68] V. Chaudhery, M. Lu, C. S. Huang, J. Polans, R. M. Tan, R. C. Zangar, and B. T. Cunningham, "Line-scanning detection instrument for photonic crystal enhanced fluorescence," *Optics Letters,* vol. 37, pp. 2565-2567, Jul 1 2012.

[69] C. S. Huang, S. George, M. Lu, V. Chaudhery, R. M. Tan, R. C. Zangar, and B. T. Cunningham, "Application of photonic crystal enhanced fluorescence to cancer biomarker microarrays," *Analytical Chemistry,* vol. 83, pp. 1425-1430, Feb 15 2011.

[70] S. George, V. Chaudhery, M. Lu, M. Takagi, N. Amro, A. Pokhriyal, Y. F. Tan, P. Ferreira, and B. T. Cunningham, "Sensitive detection of protein and miRNA cancer biomarkers using silicon-based photonic crystals and a resonance coupling laser scanning platform," *Lab on a Chip,* vol. 13, pp. 4053-4064, 2013.

[71] B. Alberts, A. Johnson, J. Lewis, M. Raff, K. Roberts, and P. Walter, "Cell junctions, cell adhesion, and the extracellular matrix," 2002.

[72] S. Kumar and V. M. Weaver, "Mechanics, malignancy, and metastasis: The force journey of a tumor cell," *Cancer Metastasis Rev,* vol. 28, pp. 113-27, 2009.